



# Production rate calibration for cosmogenic $^{10}\text{Be}$ in pyroxene by applying a rapid fusion method to $^{10}\text{Be}$ -saturated samples from the Transantarctic Mountains, Antarctica

Marie Bergelin<sup>1</sup>, Greg Balco<sup>2,1</sup>, Lee B. Corbett<sup>3</sup>, and Paul R. Bierman<sup>3</sup>

<sup>1</sup>Berkeley Geochronology Center, Berkeley, CA 94709, USA

<sup>2</sup>Lawrence Livermore National Lab, Livermore, CA 94550, USA

<sup>3</sup>Rubenstein School of the Environment and Natural Resources, University of Vermont/National Science Foundation Community Cosmogenic Facility, Burlington, VT 05405, USA

**Correspondence:** Marie Bergelin (mbergelin@bgc.org)

Received: 7 March 2024 – Discussion started: 13 March 2024

Revised: 17 June 2024 – Accepted: 23 June 2024 – Published: 15 August 2024

**Abstract.** Measurements of multiple cosmogenic nuclides in a single sample are valuable for various applications of cosmogenic nuclide exposure dating and allow for correcting exposure ages for surface weathering and erosion and establishing exposure–burial history. Here we provide advances in the measurement of cosmogenic  $^{10}\text{Be}$  in pyroxene and constraints on the production rate that provide new opportunities for measurements of multi-nuclide systems, such as  $^{10}\text{Be}/^3\text{He}$ , in pyroxene-bearing samples. We extracted and measured cosmogenic  $^{10}\text{Be}$  in pyroxene from two sets of Ferrar Dolerite samples collected from the Transantarctic Mountains in Antarctica. One set of samples has  $^{10}\text{Be}$  concentrations close to saturation, which allows for the production rate calibration of  $^{10}\text{Be}$  in pyroxene by assuming production–decay equilibrium. The other set of samples, which has a more recent exposure history, is used to determine if a rapid fusion method can be successfully applied to samples with Holocene to Last Glacial Maximum exposure ages. From measured  $^{10}\text{Be}$  concentrations in the near-saturation sample set we find the production rate of  $^{10}\text{Be}$  in pyroxene to be  $3.74 \pm 0.10$  atoms  $\text{g}^{-1} \text{yr}^{-1}$ , which is consistent with  $^{10}\text{Be}/^3\text{He}$  paired nuclide ratios from samples assumed to have simple exposure. Given the high  $^{10}\text{Be}$  concentration measured in this sample set, a sample mass of  $\sim 0.5$  g of pyroxene is sufficient for the extraction of cosmogenic  $^{10}\text{Be}$  from pyroxene using a rapid fusion method. However, for the set of samples that have low  $^{10}\text{Be}$  concentrations, measured concentrations were higher than expected. We attribute spu-

riously high  $^{10}\text{Be}$  concentrations to failure in removing all meteoric  $^{10}\text{Be}$  and/or a highly variable and poorly quantified procedural blank background correction.

## 1 Introduction

This paper describes advances in the measurement and application of cosmogenic  $^{10}\text{Be}$  in pyroxene, including a rapid fusion extraction method and a production rate calibration data set. This is important because measurements of multiple cosmogenic nuclides in single samples are valuable for various applications of exposure dating. Multiple-nuclide systematics are useful for correcting exposure ages for surface weathering and erosion (Klein et al., 1986; Nishiizumi et al., 1986; Lal, 1991) and quantifying when and how often a surface has experienced burial (Granger and Muzikar, 2001; Granger, 2006; Balco and Rovey, 2008). For quartz-rich samples, multiple-nuclide measurements ( $^{26}\text{Al}/^{10}\text{Be}/^{21}\text{Ne}$ ) in quartz are common practice and well-established (e.g., Balco and Shuster, 2009). However, multiple-nuclide measurements are generally not feasible in minerals other than quartz.

The stable cosmogenic nuclide  $^3\text{He}$  is most commonly used in mafic rocks for exposure dating, as it is retentive in both pyroxene and olivine (Blard, 2021) and easily measured using a noble gas mass spectrometer (Balter-Kennedy et al., 2020). Measurements of cosmogenic  $^{10}\text{Be}$  in pyroxene are potentially useful for exposure age applications and

have been investigated in prior studies (Balter-Kennedy et al., 2023; Blard et al., 2008; Collins, 2015; Eaves et al., 2018; Ivy-Ochs et al., 1998; Nishiizumi et al., 1990). To fully utilize paired  $^{10}\text{Be}/^3\text{He}$  in pyroxene, it is necessary to constrain the production rate of cosmogenic  $^{10}\text{Be}$  in this mineral.

Cosmogenic nuclide production rates can be quantified in samples by (i) constraining the exposure age by independent radiocarbon and/or other geological dating methods (e.g., Borchers et al., 2016; Blard et al., 2008; Eaves et al., 2018), (ii) measuring the ratio of one nuclide to another with an already well-known production rate (e.g., Niedermann et al., 2007; Luna et al., 2018), and/or (iii) measuring nuclide concentration in samples experiencing negligible erosion rates and having reached production–decay equilibrium (Borchers et al., 2016; Jull et al., 1989; Nishiizumi et al., 1986). In this study, we take advantage of some of the longest exposed rocks in central Antarctica, where erosion rates are negligible, and  $^3\text{He}$  exposure ages exceeding 8 Ma require that  $^{10}\text{Be}$  concentrations must be close to the production–decay equilibrium (Balter-Kennedy et al., 2020). This provides an opportunity to validate the previously suggested  $^{10}\text{Be}$  production rate in pyroxene constrained by the different approaches described above.

Previously, extraction of  $^{10}\text{Be}$  from pyroxene (e.g., Balter-Kennedy et al., 2023; Blard et al., 2008; Collins, 2015; Eaves et al., 2018) has used wet chemical dissolution and column chromatography similar to that for extracting  $^{10}\text{Be}$  from quartz (Corbett et al., 2016). However, this process is challenging because of the large cation load and the extremely high selectivity required in the column separation. We adopt a  $^{10}\text{Be}$  extraction method involving a total rapid fusion of the pyroxene sample (Stone, 1998) to improve the efficiency of  $^{10}\text{Be}$  extraction from pyroxene. This method is commonly used to extract meteoric  $^{10}\text{Be}$  from a variety of geologic matrices and should therefore be applicable for pyroxene despite the high concentrations of other cations.

We apply the fusion method to two sets of samples. First, we analyze a set of samples with extremely high  $^{10}\text{Be}$  concentrations ( $10^7$  atoms  $\text{g}^{-1}$ ) that, as described above, can be used for production rate calibration by assuming production–decay equilibrium. Second, we analyze an additional set of samples with much lower  $^{10}\text{Be}$  concentrations ( $10^4$ – $10^5$  atoms  $\text{g}^{-1}$ ) to determine if the fusion method can be successfully applied to samples with Holocene to Last Glacial Maximum exposure ages and much lower  $^{10}\text{Be}$  concentrations.

## 2 Method

### 2.1 Geological setting and samples

We selected two sets of samples of Ferrar Dolerite from the Transantarctic Mountains (TAM). The Ferrar Dolerite (Harvey, 2001) is a mafic intrusive rock consisting primarily of calcic plagioclase and several orthopyroxenes and

clinopyroxenes (Elliot and Fleming, 2021). The first set consists of 10 samples from high elevations in the central TAM that had previous  $^3\text{He}$  measurements indicating exposure ages  $>8$  Ma. These samples are surface boulders collected from various moraines from Roberts Massif described by Balter-Kennedy et al. (2020) and several similar samples from nearby Otway Massif (Bromley et al., 2024) (Table 1). Erosion rates for Ferrar Dolerite in Antarctica are 0–35  $\text{cm Myr}^{-1}$  (Balter-Kennedy et al., 2023). However, the  $^3\text{He}$  exposure ages limit the erosion rates for these specific samples to be  $<5$   $\text{cm Myr}^{-1}$ , and therefore this set of samples can be expected to have reached production–decay equilibrium (“saturation”) for  $^{10}\text{Be}$ , such that  $N_{10} = P_{10}/\lambda_{10}$ , where  $N_{10}$  is the  $^{10}\text{Be}$  concentration (atoms  $\text{g}^{-1}$ ),  $P_{10}$  is the  $^{10}\text{Be}$  production rate in the sample (atoms  $\text{g}^{-1} \text{yr}^{-1}$ ), and  $\lambda_{10}$  is the  $^{10}\text{Be}$  decay constant ( $4.99 \times 10^{-7} \text{yr}^{-1}$ ). After 8 Ma of exposure,  $^{10}\text{Be}$  concentrations have reached 98 % of saturation values. Thus, these samples are expected to have extremely high  $^{10}\text{Be}$  concentrations, facilitating precise measurements. Measuring  $^{10}\text{Be}$  in these samples allows a straightforward estimate of the  $^{10}\text{Be}$  production rate in pyroxene integrated over the last 8 Ma.

The second set of samples is designed to test whether or not the fusion extraction method is also effective for samples with lower  $^{10}\text{Be}$  concentrations. The samples we analyze are low-elevation glacially transported erratics near outlet glaciers of the East Antarctic Ice Sheet in northern Victoria Land. Exposure age chronologies using  $^{10}\text{Be}$  in quartz or  $^3\text{He}$  in pyroxene from the same sites indicate that these samples have exposure ages of the last glacial–interglacial cycle. In addition,  $^{10}\text{Be}$  in pyroxene was previously measured in two of these samples (MG-12 and MG-19) using a dissolution–cation exchange method by Eaves et al. (2018). We selected this set of samples in part because they had been analyzed for  $^3\text{He}$  in previous studies (Table 1). We made several additional  $^3\text{He}$  measurements so that the entire sample set now has both  $^3\text{He}$  and  $^{10}\text{Be}$  data. The  $^3\text{He}$  data provide a means of evaluating the accuracy of the  $^{10}\text{Be}$  measurements. Details of the previously analyzed samples are from Stutz et al. (2021) and Eaves et al. (2018) and are summarized in Table 1.

### 2.2 Mineral separation

The samples were crushed and sieved to a grain size of 75–125  $\mu\text{m}$  at which mostly monomineralic grains were observed. The samples were washed in water and then leached in 10 % HCl at room temperature overnight. We then ran the sample through a magnetic separator to separate pyroxene from the less magnetic plagioclase and other minerals present.

At the University of Vermont/National Science Foundation Community Cosmogenic Facility (CCF), the pyroxene grains underwent hydrofluoric acid (HF) leaching, following Balter-Kennedy et al. (2023), to remove meteoric  $^{10}\text{Be}$

**Table 1.** Location and site information for samples of Ferrar Dolerite analyzed in this study.

Sample ID	Location	Latitude (degrees)	Longitude (degrees)	Elevation (m)	Thickness (cm)	Shielding	Prior publication
15-ROB-07	Roberts Massif	−85.5249	−177.7249	2255	2.0	0.9939	Balter-Kennedy et al. (2020)
15-ROB-27	Roberts Massif	−85.5219	−177.7279	2247	4.8	0.9959	Balter-Kennedy et al. (2020)
15-ROB-30	Roberts Massif	−85.5101	−177.7943	2385	4.4	1.0000	Balter-Kennedy et al. (2020)
15-ROB-31	Roberts Massif	−85.5090	−177.7788	2369	4.3	1.0000	Balter-Kennedy et al. (2020)
15-OTW-50	Otway Massif	−85.4159	172.8086	2268	1.4	0.9967	Bromley et al. (2024)
15-OTW-55	Otway Massif	−85.4150	172.7819	2292	2.7	0.9962	Bromley et al. (2024)
15-OTW-56	Otway Massif	−85.4146	172.7756	2290	3.1	0.9959	Bromley et al. (2024)
15-OTW-57	Otway Massif	−85.4148	172.7832	2287	1.3	0.9962	Bromley et al. (2024)
15-OTW-58	Otway Massif	−85.4371	172.8626	2504	2.0	0.9980	Bromley et al. (2024)
15-OTW-60	Otway Massif	−85.4370	172.8670	2503	1.8	0.9980	Bromley et al. (2024)
17-HB-TC-02	Hughes Bluff	−75.3918	162.2125	121	1.0	0.9962	Stutz et al. (2021)
17-HB-TC-12	Hughes Bluff	−75.3957	162.2021	185	1.0	0.9919	Stutz et al. (2021)
17-EHW-05	Evans Heights	−75.0982	161.4989	433	1.0	1.0000	Stutz et al. (2021)
17-EHW-15	Evans Heights	−75.0947	161.4969	561	1.0	1.0000	Stutz et al. (2021)
15-MG12	Mackay Glacier	−76.9985	161.0376	1013	5.8	0.9790	Eaves et al. (2018)
15-MG19	Mackay Glacier	−76.9991	161.0406	981	4.0	0.9880	Eaves et al. (2018)

and any plagioclase attached to the pyroxene grains. A fine grain size reduces the amount of meteoric  $^{10}\text{Be}$  stored in the grain fractures, and HF etching was found to be sufficient to remove meteoric  $^{10}\text{Be}$  by Balter-Kennedy et al. (2023), without powdering the sample as otherwise previously suggested (Blard et al., 2008). The samples were leached in HF twice; first in a 1 L solution of 1 % HF in an ultrasonic bath at  $\sim 60^\circ\text{C}$  for 6 h and then again in 1 L of 1 % HF and 1 %  $\text{HNO}_3$  overnight, targeting a 20 %–30 % mass loss. During HF leaching, precipitates of fluoride ( $\text{MgF}_2$ ,  $\text{CaF}_2$ ) are produced and are insoluble in dilute HF. Therefore, we did a final leaching in 0.5 %  $\text{HNO}_3$  overnight in a heated ultrasonic bath to dissolve the fluoride precipitates.

### 2.3 Extraction and analyses of cosmogenic $^{10}\text{Be}$ in pyroxene

The extraction of Be was done at the CCF by total fusion in a potassium bifluoride ( $\text{KHF}_2$ ) flux according to Stone (1998). Samples were processed in two separate batches; the first batch contained the high-concentration samples, and the second batch contained the low-concentration samples. The pure pyroxene samples were powdered using a shatterbox, and 0.5 g of powdered sample was massed into 30 mL platinum crucibles. The sample mass is determined by the size of the Pt crucibles and other properties of the heating apparatus and is chosen to avoid spattering and sample loss during fusion. For the set of samples with expected high  $^{10}\text{Be}$  concentration, we added 400  $\mu\text{g}$  of  $^9\text{Be}$  carrier to each 0.5 g sample. This  $^9\text{Be}$  carrier is a beryl carrier (termed Carrier C) made at the facility with a concentration of 348  $\mu\text{g mL}^{-1}$ . After drying the sample and carrier mixture, anhydrous  $\text{KHF}_2$  and anhydrous  $\text{Na}_2\text{SO}_4$  were added at the ratio of 8 : 1 : 2

$\text{KHF}_2$  :  $\text{Na}_2\text{SO}_4$  : sample by weight to the crucibles and homogenized.

The fusion protocol at the CCF uses 30 mL platinum crucibles. While it is possible to fuse larger (1–2 g) samples in larger (100 mL) crucibles (Stone, 1998), these are not compatible with the fixed fluxing apparatus used to minimize the hazard of molten  $\text{KHF}_2$ . To increase the sample size and the measured  $^{10}\text{Be}/^9\text{Be}$  ratio for the set of expected low  $^{10}\text{Be}$  concentration samples, we fused 1 g of sample in two separate fusions of 0.5 g each, with half as much carrier (200  $\mu\text{g}$ ) as used for the initial sample batch. With sample and carrier concentrations similar in both aliquots (specifically, as close as possible with the weighing and dispensing equipment in use; we estimate better than 1 % agreement between aliquots),  $^{10}\text{Be}/^9\text{Be}$  ratios in both aliquots after fusion can be expected to be identical, so we combined them to yield a higher sample/carrier ratio than possible in a single fusion.

Before starting this procedure, we determined whether halving the amount of  $^9\text{Be}$  carrier would affect the Be yield by fusing aliquots of sample 15-OTW-60 with varying amounts of added  $^9\text{Be}$  carrier. The  $^9\text{Be}$  yields were measured by inductively coupled plasma optical emission spectroscopy (ICP-OES) at the CCF. Total  $^9\text{Be}$  yields (Table 2) show that less  $^9\text{Be}$  does not result in a lower Be yield. Because Be yields in the first set of high-concentration samples were lower than expected, we increased the amount of  $\text{Na}_2\text{SO}_4$  added to a ratio of 4 : 2 : 1  $\text{KHF}_2$  :  $\text{Na}_2\text{SO}_4$  : sample by weight as suggested for calcium-rich samples by Stone (1998). This change makes sense because the Ferrar pyroxene is calcic, and having an abundance of  $\text{SO}_4$  during fluxing suppresses the formation of  $\text{CaBeF}_4$ , which is less soluble. This modification significantly increased the total Be yield (Table 2).

After fusion, the Stone (1998) procedure involves Be and K extraction by water leaching and removal of residual fluorides by centrifuging as  $\text{BeF}_2$  is soluble and most other fluorides are not. The two aliquots of each sample were combined, and K was removed from the combined sample by precipitation of  $\text{KClO}_4$ . The supernatant was evaporated to remove the remaining  $\text{HClO}_4$  and redissolved in 12 mL of dilute  $\text{HNO}_3$ . At this point, we experienced difficulty in completely redissolving the precipitated sample and found it necessary to centrifuge the sample multiple times to remove what we presumed to be the remaining  $\text{KClO}_4$ . Although Be yields from the samples that have low  $^{10}\text{Be}$  concentrations were as expected (Balco et al., 2021), the resulting accelerator mass spectrometry (AMS) targets had unusually low beam currents, which made AMS measurement more difficult than expected (Table 2). We hypothesize that this is most likely the result of K carryover in the final stages of the extraction process and that this could have been prevented by increasing the volume of the final  $\text{HNO}_3$  solutions to dissolve K more effectively.

Ratios of  $^{10}\text{Be}/^9\text{Be}$  were measured at Lawrence Livermore National Laboratory (LLNL) and normalized to the 07KNSTD3110 standard (Nishiizumi et al., 2007) with a  $^{10}\text{Be}/^9\text{Be}$  ratio of  $2.85 \times 10^{-12}$ . Uncertainties in calculated  $^{10}\text{Be}$  concentrations include AMS measurement uncertainties, uncertainty in the Be carrier concentration, and uncertainty in blank corrections (Table 2). Five procedural blanks measured with both sample batches had a mean and standard deviation of  $128\,000 \pm 67\,000$  atoms  $^{10}\text{Be}$ . This is less than 0.4 % of the total amount of  $^{10}\text{Be}$  measured in any of the samples in the high-concentration batch (Table 2), so blank correction uncertainty makes a negligible contribution to overall measurement uncertainty for these samples. However, the highest blank values were up to 60 % of the total number of atoms measured in some of the low-concentration samples, so blank uncertainty is significant for the low-concentration batch. We discuss this in more detail in Sect. 3.5.

## 2.4 Cosmogenic $^3\text{He}$ analysis

We measured cosmogenic  $^3\text{He}$  concentrations in all samples at Berkeley Geochronology Center (BGC) following the procedure described in Balter-Kennedy et al. (2020).  $^3\text{He}$  concentrations for two samples, HB-TC-02 and HB-TC-12, have already been reported in Stutz et al. (2021). Measurements of the CRONUS-P intercomparison standard (Blard et al., 2015) during the period of these measurements were  $5.03 \pm 0.15 \times 10^9$  atoms  $\text{g}^{-1}$   $^3\text{He}$  (Balter-Kennedy et al., 2020), which is indistinguishable from the accepted value of  $5.02 \pm 0.12 \times 10^9$  atoms  $\text{g}^{-1}$  (Blard et al., 2015).

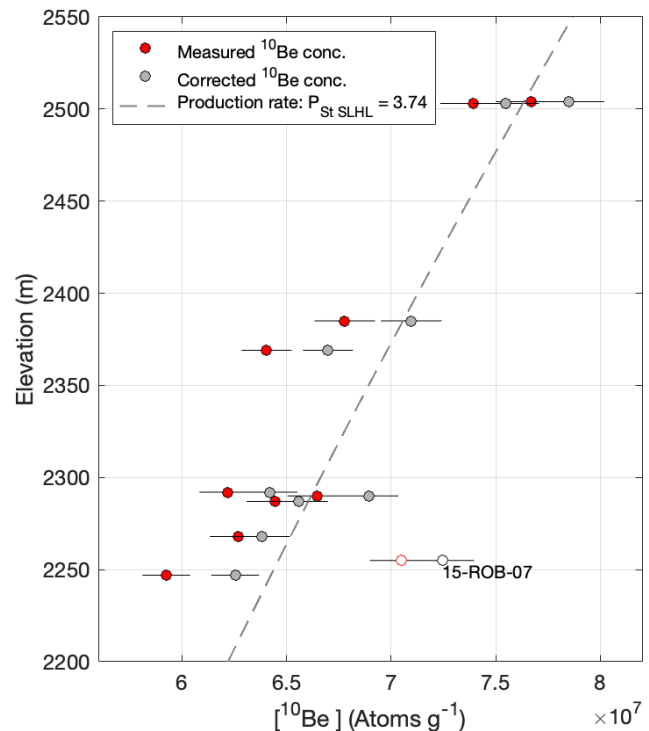


**Figure 1.** Measured  $^{10}\text{Be}$  concentrations vs. elevation. Red dots are measured  $^{10}\text{Be}$  concentrations as reported in Table 3, gray dots show measured  $^{10}\text{Be}$  concentrations corrected for sample thickness and shielding, and the dashed line shows the saturated  $^{10}\text{Be}$  concentrations for the “St” reference production rate of  $3.74 \text{ atoms g}^{-1} \text{ yr}^{-1}$   $^{10}\text{Be}$  in pyroxene. White dots indicate sample outlier, which is not included in the production rate calibration (see Sect. 3.2).

## 3 Results and discussion

### 3.1 Measured cosmogenic $^{10}\text{Be}$ in saturated samples

Measured  $^{10}\text{Be}$  concentrations in the set of high-concentration samples range from  $5.92$ – $7.67 \times 10^7$  atoms  $\text{g}^{-1}$  with uncertainties  $<2.2\%$  (Tables 2 and 3). These are equivalent to some of the highest in situ  $^{10}\text{Be}$  concentrations measured in terrestrial rocks (Spector and Balco, 2020). As expected from the elevation dependence of the  $^{10}\text{Be}$  production rate and the assumption that the  $^{10}\text{Be}$  concentrations are close to production–decay saturation, the measured concentrations increase systematically with elevation (Fig. 1).

### 3.2 The $^{10}\text{Be}$ production rate in pyroxene

In general, as discussed above,  $^3\text{He}$  exposure ages range between 8–10 Ma (5–6 times the  $^{10}\text{Be}$  half-life) and imply that  $^{10}\text{Be}$  concentrations in these samples are within 1 %–2 % of production–decay saturation. We account for the small, predicted difference from the saturation concentration by calcu-



**Table 2.** Measured Be results, including yields measured by ICP-OES in the dilute  $\text{HNO}_3$  solution prior to final precipitation, with implied Be yields for the fusion process and measured AMS currents and ratios.

Sample name	Pyroxene mass (g)	$^9\text{Be}$ added ( $\mu\text{g}$ )	Be yield ( $\mu\text{g}$ )	Be yield (%)	AMS $^{10}\text{Be}/^9\text{Be}$	Mean $^9\text{Be}$ current relative to standard <sup>a</sup>	Measured $^{10}\text{Be}$ ( $10^6$ atoms)	Measured $^{10}\text{Be}$ conc. <sup>b</sup> ( $10^6$ atoms $\text{g}^{-1}$ )
High-concentration batch								
15-ROB-07	0.493	403	110	27	$1.281 \pm 0.024 \times 10^{-12}$	0.48	$34.89 \pm 0.75$	$70.5 \pm 1.5$
15-ROB-27	0.497	403	118	29	$1.085 \pm 0.018 \times 10^{-12}$	0.54	$29.57 \pm 0.56$	$59.2 \pm 1.1$
15-ROB-30	0.488	402	145	36	$1.222 \pm 0.023 \times 10^{-12}$	0.55	$33.21 \pm 0.70$	$67.8 \pm 1.4$
15-ROB-31	0.501	400	132	33	$1.192 \pm 0.018 \times 10^{-12}$	0.66	$32.21 \pm 0.59$	$64.0 \pm 1.2$
15-OTW-50	0.498	398	117	30	$1.165 \pm 0.022 \times 10^{-12}$	0.59	$31.34 \pm 0.67$	$62.7 \pm 1.3$
15-OTW-55	0.496	402	117	29	$1.139 \pm 0.021 \times 10^{-12}$	0.47	$30.96 \pm 0.66$	$62.2 \pm 1.3$
15-OTW-56	0.498	399	108	27	$1.232 \pm 0.023 \times 10^{-12}$	0.53	$33.23 \pm 0.70$	$66.5 \pm 1.4$
15-OTW-57	0.490	397	113	28	$1.182 \pm 0.022 \times 10^{-12}$	0.60	$31.71 \pm 0.67$	$64.5 \pm 1.4$
15-OTW-58	0.501	399	107	27	$1.429 \pm 0.028 \times 10^{-12}$	0.50	$38.56 \pm 0.85$	$76.7 \pm 1.7$
15-OTW-60	0.497	398	114	29	$1.369 \pm 0.026 \times 10^{-12}$	0.47	$36.87 \pm 0.78$	$73.9 \pm 1.6$
15-OTW-60-150 <sup>c</sup>	0.493	159	64	40	–	–	–	–
15-OTW-60-250 <sup>c</sup>	0.495	258	79	31	–	–	–	–
Blank (129-BLK)	–	398	279	70	$5.1 \pm 1.0 \times 10^{-15}$	0.80	$0.139 \pm 0.028$	–
Blank (129-BLKX)	–	404	267	66	$5.28 \pm 0.48 \times 10^{-15}$	0.62	$0.144 \pm 0.013$	–
Blank (129-0BLK)	–	402	297	74	$2.18 \pm 0.27 \times 10^{-15}$	0.79	$0.0594 \pm 0.0074$	–
Low-concentration batch								
17-HB-TC-02	0.998	400	268	67	$2.53 \pm 0.11 \times 10^{-14}$	0.49	$0.685 \pm 0.030$	$0.558 \pm 0.074$
17-HB-TC-12	0.997	400	250	63	$2.03 \pm 0.11 \times 10^{-14}$	0.36	$0.550 \pm 0.030$	$0.424 \pm 0.074$
17-EHW-05	0.998	399	242	61	$1.67 \pm 0.13 \times 10^{-14}$	0.22	$0.451 \pm 0.034$	$0.323 \pm 0.075$
17-EHW-15	0.999	399	267	67	$3.70 \pm 0.17 \times 10^{-14}$	0.27	$0.997 \pm 0.046$	$0.87 \pm 0.082$
15-MG12	1.001	398	281	71	$2.40 \pm 0.13 \times 10^{-14}$	0.32	$0.646 \pm 0.037$	$0.517 \pm 0.076$
15-MG19	1.000	399	263	66	$3.96 \pm 0.55 \times 10^{-14}$	0.10	$1.07 \pm 0.15$	$0.94 \pm 0.16$
Blank (130-BLK)	–	399	333	83	$8.3 \pm 1.2 \times 10^{-15}$	0.17	$0.226 \pm 0.032$	–
Blank (130-BLKX)	–	399	333	83	$2.62 \pm 0.54 \times 10^{-15}$	0.25	$0.071 \pm 0.015$	–

<sup>a</sup> Mean current for the KNSTD3110 is 21.5  $\mu\text{A}$ . <sup>b</sup> The measured  $^{10}\text{Be}$  concentrations include blank correction. <sup>c</sup> Samples were processed only as a yield test, and no AMS measurements were made.

**Table 3.** The  $^3\text{He}$  and  $^{10}\text{Be}$  concentrations for long-exposure glacial erratics in the Transantarctic Mountains. The  $^{10}\text{Be}$  production rate is determined from Eq. (1).

Sample ID	$^{10}\text{Be}$ conc. ( $10^9$ atoms g)	$^3\text{He}$ conc. <sup>a</sup> ( $10^9$ atoms g)	$^3\text{He}$ exposure age <sup>b</sup> (Myr)	$^{10}\text{Be}$ production rate SLHL spallation <sup>c</sup> (atoms $\text{g}^{-1}$ $\text{yr}^{-1}$ )	$^3\text{He}$ data from
15-ROB-07	$7.05 \pm 0.15$	$9.18 \pm 0.11$	$8.12 \pm 0.16$	$4.256 \pm 0.093$	Balter-Kennedy et al. (2020)
15-ROB-27	$5.92 \pm 0.11$	$9.05 \pm 0.10$	$8.265 \pm 0.094$	$3.687 \pm 0.072$	Balter-Kennedy et al. (2020)
15-ROB-30	$6.78 \pm 0.14$	$12.22 \pm 0.12$	$9.95 \pm 0.29$	$3.776 \pm 0.081$	Balter-Kennedy et al. (2020)
15-ROB-31	$6.40 \pm 0.12$	$10.527 \pm 0.090$	$8.67 \pm 0.12$	$3.624 \pm 0.068$	Balter-Kennedy et al. (2020)
15-OTW-50	$6.27 \pm 0.13$	$10.87 \pm 0.17$	$9.40 \pm 0.23$	$3.683 \pm 0.079$	Bromley et al. (2024)
15-OTW-55	$6.22 \pm 0.13$	$11.04 \pm 0.18$	$9.56 \pm 0.11$	$3.641 \pm 0.078$	Bromley et al. (2024)
15-OTW-56	$6.65 \pm 0.14$	$10.508 \pm 0.093$	$9.14 \pm 0.12$	$3.925 \pm 0.084$	Bromley et al. (2024)
15-OTW-57	$6.45 \pm 0.14$	$10.84 \pm 0.13$	$9.28 \pm 0.13$	$3.739 \pm 0.080$	Bromley et al. (2024)
15-OTW-58	$7.67 \pm 0.17$	$12.42 \pm 0.18$	$9.05 \pm 0.14$	$3.876 \pm 0.087$	Bromley et al. (2024)
15-OTW-60	$7.39 \pm 0.16$	$11.73 \pm 0.23$	$8.54 \pm 0.17$	$3.742 \pm 0.081$	Bromley et al. (2024)

<sup>a</sup> For samples where more than one measurement exist the concentration represents the error-weighted mean and the standard error. <sup>b</sup> The uncertainty in the age is the internal uncertainty using the online exposure age calculator. <sup>c</sup> The sea level/high-latitude (SLHL) reference  $^{10}\text{Be}$  production rate is determined from Eq. (1) and the scaling method of Stone (2000), as implemented in Balco et al. (2008).

lating the production rate as follows:

$$P_{10} = \frac{N_{10} \lambda_{10}}{(1 - e^{-\lambda_{10} t_3})}, \quad (1)$$

where  $P_{10}$  is the  $^{10}\text{Be}$  production rate in the sample (atoms  $\text{g}^{-1}$   $\text{yr}^{-1}$ ),  $N_{10}$  is the  $^{10}\text{Be}$  concentration (atoms  $\text{g}^{-1}$ ),  $\lambda_{10}$  is the  $^{10}\text{Be}$  decay constant ( $4.99 \times 10^{-7}$   $\text{yr}^{-1}$ ), and  $t_3$  is

the  $^3\text{He}$  exposure age (yr). Because the samples are close to production–decay saturation, the production rate determined from Eq. (1) is insensitive to uncertainty in the assumed exposure age. Therefore, although we use the apparent  $^3\text{He}$  exposure ages to correct for an inferred small systematic difference from production–decay saturation, the accuracy of the  $^3\text{He}$  ages is minimally important for the  $^{10}\text{Be}$  production

rate estimate. To obtain the spallogenic production rate of  $^{10}\text{Be}$  in pyroxene, we subtract the production rate in pyroxene due to muons using the muon interaction cross-sections of Balter-Kennedy et al. (2023), which account for <1 % of the production rate, and correct for sample thickness and topographic shielding.

Applying the “St” elevation scaling of Stone (2000) then yields sea level/high-latitude (SLHL) production rates in the range of 3.6–4.3 atoms  $\text{g}^{-1} \text{yr}^{-1}$  (Table 3). The  $^{10}\text{Be}$  production rate increases with elevation, so samples near or at saturation are expected to likewise have  $^{10}\text{Be}$  concentrations increasing with elevation. This is true for all samples, except 15-ROB-07, which has an excess  $^{10}\text{Be}$  concentration equivalent to  $\sim 250 \text{ m}$  (Fig. 1). Removing one outlier (15-ROB-07; see Fig. 1) yields a mean and standard error of  $3.74 \pm 0.10$  atoms  $\text{g}^{-1} \text{yr}^{-1}$ .

The production rate estimate agrees with that of Balter-Kennedy et al. (2023) ( $3.6 \pm 0.2$  atoms  $\text{g}^{-1} \text{yr}^{-1}$ ), which was cross-calibrated with the  $^3\text{He}$  production rate. However, in the present study, our calibration is independent of the  $^3\text{He}$  production rate, where samples with near-saturated  $^{10}\text{Be}$  concentrations permit a direct calculation of the production rate from the measurements. In contrast, the sample set in the Balter-Kennedy et al. (2023) study lacks direct constraints on the exposure age and/or exposure history, and a best-fit production rate was computed from values that permitted all the samples to have a simple exposure history bounded by limiting assumptions of steady exposure at zero erosion and steady erosion for an infinite time. While they are not directly comparable, it is possible to determine whether the two data sets are consistent with each other and with the assumption of simple exposure. In Fig. 2 we construct a  $^{10}\text{Be}/^3\text{He}$  two-nuclide diagram using the production rate determined from our study and an assumed  $^3\text{He}$  production rate of 120 atoms  $\text{g}^{-1} \text{yr}^{-1}$  (Borchers et al., 2016), and plot the  $^{10}\text{Be}/^3\text{He}$  data from both studies. This shows that all data from both studies (except for one outlier in our study identified above) plot within the simple exposure region and are therefore internally consistent.

Finally, we consider whether our data are consistent with other  $^{10}\text{Be}$ -in-pyroxene production rate calibration data and with commonly used production rate scaling methods. Two other studies obtained  $^{10}\text{Be}$ -in-pyroxene production rate calibration data from samples with independent age constraints. Blard et al. (2008) included two samples (SI41 and SI43) from separate lava flows at Mount Etna, Italy, with K/Ar ages of 33 and 10 kyr, respectively. Eaves et al. (2018) obtained three samples from the Murimotu formation debris avalanche at Mount Ruapehu, New Zealand, which has a radiocarbon age of 10.5 kyr. In Fig. 3, we apply the production rate calibration code from version 3 of the online exposure age calculator originally described by Balco et al. (2008) and subsequently updated to (i) our production rate calibration data alone and (ii) our data with the Blard et al. (2008) and Eaves et al. (2018) data. One aspect of this comparison is

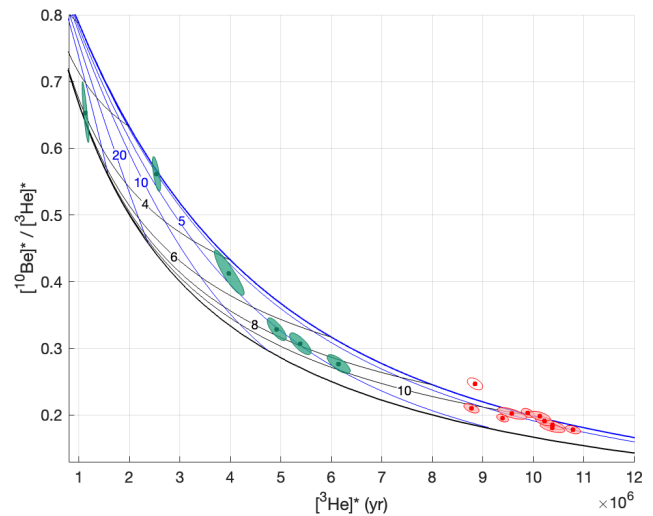


**Figure 2.** A  $^{10}\text{Be}$ - $^3\text{He}$  two-nuclide diagram. Red data points show measurements from this study, green data points are from Balter-Kennedy et al. (2023), and each shaded ellipse represents the 68 % confidence interval in the measured nuclide concentrations. The thick blue line is the simple exposure line, and the thin blue lines are lines of constant erosion ( $\text{m Myr}^{-1}$ ). The thick black line is the steady-erosion line, and the thin black lines are constant-age lines ( $\text{Myr}$ ). \* signifies nuclide concentrations normalized to site-specific production rate for comparison across sampling locations.

that our data are from relatively high elevations and high latitudes, and the other calibration data are from relatively low elevations and moderate latitudes.

The production rate of  $^{10}\text{Be}$  in pyroxene is predicted to vary with the major element composition of the target mineral. Element-specific production rates calculated by Masarik (2002) predict up to a possible 27 % variation between the extreme end member pyroxene compositions (enstatite vs. ferrosilite). However, the variation among the composition of pyroxene in which  $^{10}\text{Be}$  concentrations have been measured is much less, as the mineral separation process used to prepare samples for  $^{10}\text{Be}$  analysis does not select for individual pyroxenes. Using the element-specific predictions from Masarik, the full range of pyroxene compositions observed in the Ferrar Dolerite (Elliot and Fleming, 2021) predicts a maximum 6.5 % variation in the production rate. Pyroxene compositions in our high-concentration sample set used for production rate calibration (Table 4) predict a maximum production rate difference of 5 % and a standard deviation of 2 % (Table 4). Furthermore, pyroxene compositions in previous production rate calibration studies (Blard et al., 2008; Collins, 2015) fall within the range predicted for Ferrar pyroxenes. Thus, although variations in production rates due to pyroxene composition may be important in some situations, they are likely at the level of measurement uncertainty for available calibration data.

Taken together, we find that the reference production rate of  $3.74 \pm 0.10$  atoms  $\text{g}^{-1} \text{yr}^{-1}$  determined in this study is

**Table 4.** Major element composition (oxide wt %) and theoretically simulated SLHL  $^{10}\text{Be}$  production rate in pyroxene.

Sample name	SiO <sub>2</sub> (wt %)	TiO <sub>2</sub> (wt %)	Al <sub>2</sub> O <sub>3</sub> (wt %)	FeO <sup>a</sup> (wt %)	MnO (wt %)	MgO (wt %)	CaO (wt %)	Na <sub>2</sub> O (wt %)	K <sub>2</sub> O (wt %)	P <sub>2</sub> O <sub>5</sub> (wt %)	Theoretical $^{10}\text{Be}$ production rate relative to mean
15-ROB-07	53.2	0.75	1.08	19.4	0.381	15.0	10.0	0.10	0.087	0.0010	1.012
15-ROB-27	52.7	1.23	1.15	20.7	0.405	13.7	9.9	0.14	0.094	–	1.003
15-ROB-30	50.5	2.43	1.49	25.6	0.466	9.2	9.9	0.22	0.186	0.0006	0.968
15-ROB-31	49.5	1.86	1.30	26.8	0.494	9.4	10.4	0.18	0.108	0.0002	0.960
15-OTW-50	52.3	1.01	1.35	18.8	0.391	14.2	11.8	0.12	0.080	–	1.005
15-OTW-55	53.5	0.68	1.20	18.0	0.381	14.8	11.3	0.09	0.056	0.0003	1.014
15-OTW-56	52.9	0.95	1.24	19.5	0.403	13.5	11.4	0.09	0.065	0.0008	1.004
15-OTW-57	52.7	0.87	1.15	18.4	0.391	14.7	11.7	0.07	0.029	0.0001	1.009
15-OTW-58	53.5	0.76	1.25	18.3	0.381	14.8	10.9	0.12	0.054	0.0003	1.014
15-OTW-60	52.7	0.64	1.15	18.7	0.387	15.1	11.2	0.08	0.030	0.0005	1.010

<sup>a</sup> Total Fe expressed as FeO. <sup>b</sup> The theoretical production rate is calculated from the Masarik (2002) formula for estimating the compositional dependence of the  $^{10}\text{Be}$  production rate in pyroxene and results in a mean value of 4.55 and standard deviation of 0.09 atoms  $\text{g}^{-1} \text{yr}^{-1}$ . Note that although the inter-element variation in predicted production rates in this study is expected to be accurate, the absolute value of the production rate (e.g., the value of 4.55 atoms  $\text{g}^{-1} \text{yr}^{-1}$ ) was calculated by reference to obsolete  $^{10}\text{Be}$  measurement standards and is not expected to be accurate.

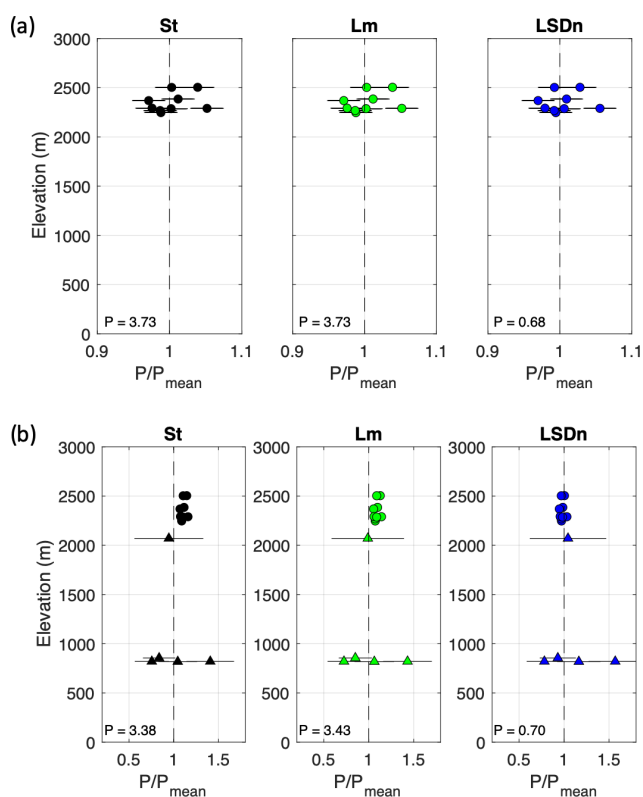


**Figure 3.** Relative variation with elevation in production rate scaling parameters calculated from calibration samples in this study (high-elevation data; shown in panels **a** and **b** as circles) and those of Blard et al. (2008) and Eaves et al. (2018) (lower-elevation data; shown in panel **b** only as triangles). For the “St” and “Lm” scaling methods, the production rate scaling parameter  $P$  is a reference production rate with units of atoms per gram per year; for the “LSDn” scaling method, it is a non-dimensional correction factor. Note that the  $x$ -axis limits are different in **(a)** and **(b)**. The reference production rate ( $P$ ) value for each scaling factor is the calculated site-weighted mean.

consistent with other  $^{10}\text{Be}$ -in-pyroxene production rate calibration data (Blard et al., 2008; Eaves et al., 2018) and in agreement with the previously published production rate of  $3.6 \pm 0.2$  atoms  $\text{g}^{-1} \text{yr}^{-1}$  (Balter-Kennedy et al., 2023) with an overall improvement in the uncertainty.

### 3.3 The $^{10}\text{Be}$ and $^3\text{He}$ measurements in low-concentration samples

The  $^{10}\text{Be}$  concentrations from the set of young-exposure-age erratics, as expected, were 2 orders of magnitude lower than concentrations in the high-elevation, saturated samples (Table 5). As discussed above, these samples are glacially transported erratics found near the margins of major glaciers in the Transantarctic Mountains. The geomorphic context,  $^3\text{He}$  exposure ages on these and nearby samples, and  $^{10}\text{Be}$  exposure ages on nearby quartz-bearing samples, all indicate that these samples were emplaced by deglaciation during the last glacial–interglacial cycle and have most likely not experienced more than 50 000 years of exposure (Stutz et al., 2021; Eaves et al., 2018).

Given the assumptions that (i) the samples have experienced exposure only in the last  $\sim 50$  000 years and (ii) the non-cosmogenic  $^3\text{He}$  concentration is constant among samples, measured  $^3\text{He}$  and  $^{10}\text{Be}$  concentrations should be linearly related, with a slope given by the  $^3\text{He}/^{10}\text{Be}$  production ratio and an intercept on the  $^3\text{He}$  axis given by the non-cosmogenic  $^3\text{He}$  concentration in Ferrar pyroxene. Non-cosmogenic  $^3\text{He}$  in Ferrar pyroxene is most likely derived from nucleogenic production and has been estimated in various studies to be less than approximately  $6 \times 10^6$  atoms  $\text{g}^{-1}$  (Eaves et al., 2018; Kaplan et al., 2017; Margerison et al., 2005).

Combining our  $^3\text{He}$  measurements with the  $^{10}\text{Be}$  concentrations obtained from Collins (2015) and Eaves et al. (2018) results in the expected linear relationship, with a slope of  $^3\text{He}/^{10}\text{Be} = 28.5 \pm 4.6$  and  $^3\text{He}$  intercept of

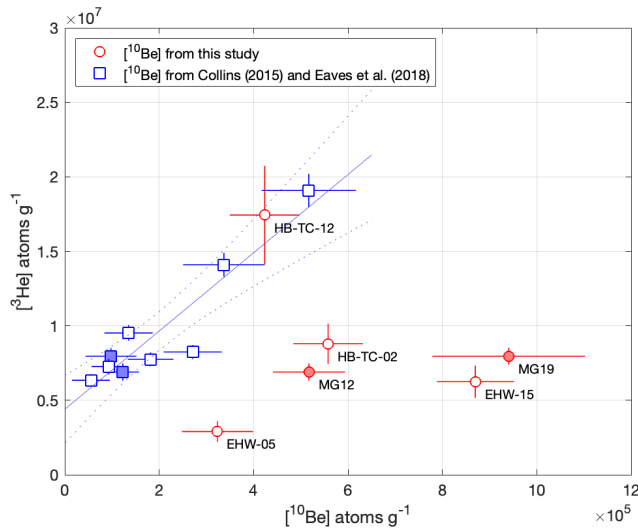


**Figure 4.** Measured  $^{10}\text{Be}$  and  $^3\text{He}$  concentrations in low-concentration samples. Red dots are sample data with  $^{10}\text{Be}$  concentrations measured in this study. Blue squares are sample data with  $^{10}\text{Be}$  concentrations obtained from Collins (2015) and Eaves et al. (2018). Solid points represent samples that have duplicated  $^{10}\text{Be}$  measurements from this study and Eaves et al. (2018). The horizontal and vertical lines associated with each data point are the measured uncertainties in the nuclide concentrations. The solid blue line is the York regression linear relationship for the blue data points only with a 95 % confidence bound (dashed blue lines).

$3.9 \pm 0.8 \times 10^6$  atoms  $\text{g}^{-1}$  (Fig. 4). If we take the reference  $^3\text{He}$  production rate to be  $120 \pm 13$  atoms  $\text{g}^{-1} \text{yr}^{-1}$ , which is derived for “St” scaling with the calibration data set of Borchers et al. (2016), this slope implies a  $^{10}\text{Be}$  production rate of  $4.20 \pm 0.82$  atoms  $\text{g}^{-1} \text{yr}^{-1}$ , which is consistent with, albeit less precise than, the other estimates discussed in the previous sections. The  $^3\text{He}$  intercept is most likely a good estimate of the nucleogenic  $^3\text{He}$  concentration in Ferrar pyroxene.

However, only one of the  $^{10}\text{Be}$  concentrations measured in this study agrees with the expected linear relationship; the others are systematically higher than expected, by hundreds of thousands of atoms per gram. In particular, MG12 and MG19 were measured both by Eaves et al. (2018) and in this study; our results are  $3.94 \times 10^5$  and  $8.4 \times 10^5$  atoms  $\text{g}^{-1}$  higher than those of Eaves et al. (2018), respectively (Table 5). Two possible explanations for this discrepancy are (i) failure to completely remove meteoric  $^{10}\text{Be}_m$  before extraction or (ii) a highly variable and poorly quantified procedural blank background correction (Table 2). Both scenarios are discussed in the following sections.

### 3.4 Removal of meteoric $^{10}\text{Be}$

Failure to successfully remove all meteoric  $^{10}\text{Be}_m$  during HF etching would result in spuriously high concentrations of pre-

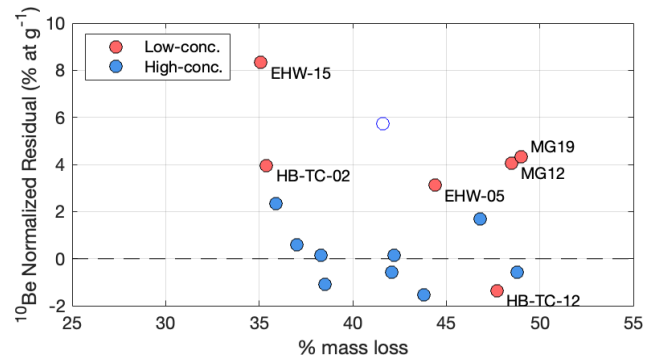


**Figure 5.** Comparison of mass lost during HF etching with normalized residuals between measured  $^{10}\text{Be}$  concentrations in samples and expected concentrations. For the high-concentration samples (blue), the expected values are given by the dashed line in Fig. 1. For the low-concentration samples (red), the expected values are given by the linear regression in Fig. 4. The white dot represents the outlier as discussed in Fig. 1.

sumed cosmogenic  $^{10}\text{Be}$ . Balter-Kennedy et al. (2023) found that when using fine to medium grains of pyroxene (32–125  $\mu\text{m}$ ),  $\sim 25$  % mass loss after leaching a sample in 1 % HF/1 %  $\text{HNO}_3$  is sufficient to remove meteoric  $^{10}\text{Be}_m$ . After leaching, we observed 35 %–49 % mass loss, indicating that leaching should have been sufficient. Figure 5 compares the mass lost during HF etching to the residual between the measured and predicted in situ cosmogenic  $^{10}\text{Be}$  concentration (atoms  $\text{g}^{-1}$ ), normalized to the error in measured concentrations and calculated using the production rate from this study of  $3.74$  atoms  $\text{g}^{-1} \text{yr}^{-1}$  and the minimum  $^3\text{He}$  ages for both the high- and low-concentration samples. We see no clear relationship between mass loss and the  $^{10}\text{Be}$  residual for either of the two sample sets, as expected. This is especially evident in samples HB-TC-12 and MG19, which both display similar mass loss ( $\sim 48$  %).

If we were to assume that the increased  $^{10}\text{Be}$  is solely meteoric, then that contributes  $\sim 6 \times 10^5$  atoms  $\text{g}^{-1}$ . This is estimated from the average difference between the  $^{10}\text{Be}$  concentrations measured for the replicated samples from this study and those from Eaves et al. (2018), which is assumed to be free of meteoric  $^{10}\text{Be}$  (Table 5). Such contribution would account for less than 1 % of the  $^{10}\text{Be}$  concentration measured for the set of high-concentration samples used for estimating the production rate of  $^{10}\text{Be}$  in pyroxene. Therefore, any potential contribution from meteoric  $^{10}\text{Be}$  would most likely have an insignificant impact on the reference production rate reported in Sect. 3.2.

As dissolved plagioclase attached to pyroxene grains contributes to the total mass loss after leaching, the total mass loss is not a direct reflection of the mass of pyroxene lost that is presumed to contain meteoric  $^{10}\text{Be}_m$ . While the  $>35$  % mass loss is mostly pyroxene, some unknown fraction could be from plagioclase. We can therefore not exclude that sam-



**Table 5.** Measured  $^3\text{He}$  and  $^{10}\text{Be}$  concentrations in low-concentration samples from glacial transported erratics during the last glacial-interglacial cycle, including published concentrations from others.

Sample name	Aliquot	Mass (g)	Measured $^4\text{He}$ ( $10^9$ atoms $\text{g}^{-1}$ )	Total measured $^3\text{He}$ ( $10^6$ atoms $\text{g}^{-1}$ )	Total $^3\text{He}$ -weighted mean ( $10^6$ atoms $\text{g}^{-1}$ )	$^3\text{He}$ data source	Measured $^{10}\text{Be}$ ( $10^6$ atoms $\text{g}^{-1}$ )	$^{10}\text{Be}$ data source
Mt. Gran (Mackay Glacier)								
MG-01	a	0.03887	$34.3 \pm 1.2$	$5.88 \pm 0.77$	$6.36 \pm 0.42$	This paper		
	b	0.09641	$35.3 \pm 1.3$	$6.56 \pm 0.50$				
							$0.055 \pm 0.040$	Eaves et al. (2018)
MG-02B	a	0.04679	$159.1 \pm 5.7$	$8.40 \pm 0.85$	$8.26 \pm 0.48$	This paper		
	b	0.08192	$158.4 \pm 5.6$	$8.15 \pm 0.69$				
	c	0.04119	$154.6 \pm 5.6$	$8.3 \pm 1.1$				
							$0.271 \pm 0.062$	Collins (2015)
MG-07	a	0.06049	$34.7 \pm 1.2$	$14.13 \pm 0.80$	$14.13 \pm 0.80$	This paper	$0.337 \pm 0.087$	Eaves et al. (2018)
MG-08B	b	0.01779	$131.1 \pm 4.7$	$22.3 \pm 2.4$	$19.13 \pm 1.12$	This paper		
	c	0.04954	$295.4 \pm 10.6$	$18.3 \pm 1.3$				
							$0.52 \pm 0.10$	Collins (2015)
MG-15	a	0.09931	$84.9 \pm 3.0$	$8.52 \pm 0.63$	$7.77 \pm 0.46$	This paper		
	b	0.07935	$81.3 \pm 2.9$	$6.90 \pm 0.67$				
							$0.182 \pm 0.048$	Eaves et al. (2018)
MG-22	a	0.09661	$29.1 \pm 1.0$	$7.34 \pm 0.61$	$7.28 \pm 0.53$	This paper		
	b	0.03488	$28.1 \pm 1.0$	$7.1 \pm 1.0$				
							$0.093 \pm 0.036$	Eaves et al. (2018)
MG-32	a	0.09666	$36.5 \pm 1.3$	$9.99 \pm 0.62$	$9.54 \pm 0.53$	This paper		
	b	0.03643	$38.0 \pm 1.4$	$8.3 \pm 1.0$				
							$0.135 \pm 0.051$	Eaves et al. (2018)
MG-12	a	0.02253	$174.1 \pm 1.5$	$7.29 \pm 0.88$	$6.56 \pm 1.02$	This paper		
	b	0.01526	$243.9 \pm 2.1$	$5.4 \pm 1.6$				
	c	0.02199	$165.4 \pm 1.4$	$6.98 \pm 0.87$				
							$0.123 \pm 0.034$	Eaves et al. (2018)
							$0.517 \pm 0.076$	This paper
MG-19	a	0.02329	$583.7 \pm 4.9$	$7.2 \pm 1.0$	$7.78 \pm 2.32$	This paper		
	c	0.02600	$590.9 \pm 4.9$	$10.7 \pm 1.0$				
	d	0.01643	$602.0 \pm 4.9$	$6.0 \pm 1.3$				
	e	0.01431	$525.2 \pm 4.4$	$9.7 \pm 1.7$				
	f	0.01403	$490.1 \pm 4.1$	$5.3 \pm 1.5$				
							$0.098 \pm 0.054$	Eaves et al. (2018)
							$0.94 \pm 0.16$	This paper
Evans Heights (David Glacier)								
EHW-05	a	0.02364	$108.6 \pm 1.8$	$3.8 \pm 1.7$	$2.91 \pm 0.7$	This paper		
	b	0.06775	$108.0 \pm 1.9$	$4.43 \pm 0.87$				
	c	0.05934	$107.7 \pm 1.9$	$1.60 \pm 0.75$				
							$0.323 \pm 0.075$	This paper
EHW-15	a	0.02905	$216.5 \pm 3.7$	$6.9 \pm 1.5$	$6.3 \pm 1.1$	This paper		
	b	0.03577	$179.9 \pm 3.1$	$4.4 \pm 1.4$				
	c	0.03328	$178.3 \pm 3.1$	$7.7 \pm 1.5$				
							$0.870 \pm 0.082$	This paper
Hughes Bluff (David Glacier)								
HB-TC-02	a	0.02268	$230.0 \pm 5.5$	$11.9 \pm 2.1$	$8.8 \pm 1.4$	Stutz et al. (2021)		
	b	0.03491	$195.9 \pm 3.4$	$8.2 \pm 1.7$				
	c	0.03291	$178.9 \pm 3.1$	$7.5 \pm 1.7$				
							$0.558 \pm 0.074$	This paper
HB-TC-12	c	0.01439	$99.2 \pm 1.7$	$17.5 \pm 3.3$	$17.5 \pm 3.3$	Stutz et al. (2021)	$0.424 \pm 0.074$	This paper

All  $^3\text{He}$  measurements employed the BGC "Ohio" NGMS system. Analytical methods are as described in Balter-Kennedy et al. (2020). The  $^{10}\text{Be}$  data from Eaves et al. (2018) and Collins (2015) were originally normalized to the NIST SRM4325 standard with an assumed  $^{10}\text{Be}/^9\text{Be}$  ratio of  $3 \times 10^{-11}$  and have been renormalized to the "07KNSTD" standardization of Nishiizumi et al. (2007).

ples may contain some meteoric  $^{10}\text{Be}_m$ . However, the lack of correlation between the residuals vs. expected values and the mass loss during etching makes it unlikely that the systematically measured excess in  $^{10}\text{Be}$  concentration is solely caused by meteoric  $^{10}\text{Be}_m$ .

### 3.5 Uncertainty in the blank correction

The blank correction may be one of the major challenges for analyzing low  $^{10}\text{Be}$  concentration samples, and a highly variable blank could cause a scatter and increase in measured  $^{10}\text{Be}$  concentrations that we observed. The blank correction value is obtained from the average of all five blanks processed during both the high- and low-concentration sample sets. However, the blanks are highly variable between 71 000 and 288 000  $^{10}\text{Be}$  atoms, which accounts for 10%–60% of the total measured  $^{10}\text{Be}$  atoms in the low-concentration batch. If we assume a blank of 71 000  $^{10}\text{Be}$  atoms for sample HB-TC-02, we get a corrected  $^{10}\text{Be}$  concentration of  $6.15 \times 10^5 \text{ atoms g}^{-1}$ . However, if we assume a blank of 288 000  $^{10}\text{Be}$  atoms, we get a  $^{10}\text{Be}$  concentration of  $3.97 \times 10^5 \text{ atoms g}^{-1}$ , a significantly lower  $^{10}\text{Be}$  concentration. Thus, variability in the measurement background may account for a significant fraction of the difference between measured and expected concentrations. It would only be possible to quantify this contribution of  $^{10}\text{Be}$  by measuring additional blanks and replicates of low-concentration samples.

### 3.6 Limitations in extracting cosmogenic $^{10}\text{Be}$ from pyroxene by fusion

Agreement of our production rate estimate from saturated samples with all other existing data shows that extraction of cosmogenic  $^{10}\text{Be}$  from pyroxene by total rapid fusion is effective and accurate for samples with high  $^{10}\text{Be}$  concentrations. Previous studies of  $^{10}\text{Be}$  in pyroxene used wet chemical dissolution and ion exchange chromatography, similar to the procedure used in extracting  $^{10}\text{Be}$  from quartz. However, concentrations of the major cations Ca, Fe, Mg, and Na are much greater in pyroxene than the trace levels found in quartz, which requires substantial scaling up of ion exchange columns (Eaves et al., 2018). The total fusion method of Stone (1998), having extremely high selectivity for Be relative to these cations, completely avoids this issue. However, we were not able to sufficiently scale up the rapid fusion method to obtain the desired signal-to-noise ratio during AMS analysis for the lower-concentration samples.

#### 3.6.1 Sample size limitations

The main obstacle to measuring cosmogenic  $^{10}\text{Be}$  in pyroxene at low concentrations is the difficulty in increasing the sample size to obtain a higher  $^{10}\text{Be}/^9\text{Be}$  ratio and thus signal-to-background ratio. This is a challenge for both extraction methods, albeit for different reasons. For young-exposure-

age samples (5–33 kyr), Eaves et al. (2018) dissolved 1.1–2.8 g of pyroxene using large ion exchange columns. For our extraction by total fusion, the sample size is limited to 0.5 g by the size of the Pt crucibles. Note that Stone (1998) processed samples up to 4 g using 100 mL crucibles.

As discussed above, to address the crucible size limitation, we merged duplicate samples of 0.5 g to obtain a total sample mass of 1 g, but increasing the amount of K present in the final steps of the procedure most likely resulted in incomplete separation of K from Be. This, in turn, may have suppressed AMS beam currents (Table 2) and resulted in poor measurement precision for some samples. This could likely be corrected by increasing solution volumes in some steps of the procedure and repeating various precipitation steps to ensure the complete removal of K.

## 4 Conclusion

In this study, we provide advances in the measurement and application of cosmogenic  $^{10}\text{Be}$  in pyroxene by applying a rapid fusion extraction method (Stone, 1998) and a production rate calibration data set. We extracted and measured cosmogenic  $^{10}\text{Be}$  in pyroxene from two sets of Ferrar Dolerite samples. One set of samples consisting of 10 high-elevation boulders collected from moraines in the upper TAM have  $^3\text{He}$  measurements indicating that these samples have  $^{10}\text{Be}$  concentration close to saturation. We use this sample set to calibrate the production rate of  $^{10}\text{Be}$  in pyroxene by assuming production–decay equilibrium. The other set of samples consisting of six low-elevation glacially transported erratics from northern Victoria Land are used to test whether or not a rapid fusion extraction method is feasible for samples that have low  $^{10}\text{Be}$  concentrations.

From measured  $^{10}\text{Be}$  concentrations in the near-saturation sample set we find the production rate of  $^{10}\text{Be}$  in pyroxene to be  $3.74 \pm 0.10 \text{ atoms g}^{-1} \text{ yr}^{-1}$ , which is in agreement with previously published production rates (Balter-Kennedy et al., 2023; Eaves et al., 2018; Blard et al., 2008), and consistent with  $^{10}\text{Be}/^3\text{He}$  paired nuclide ratios from samples assumed to have simple exposure. Given the high  $^{10}\text{Be}$  concentration measured, a sample mass of  $\sim 0.5 \text{ g}$  of pyroxene with 400  $\mu\text{g}$  added  $^9\text{Be}$  carrier is sufficient for obtaining meaningful  $^{10}\text{Be}/^9\text{Be}$  ratios well above blank levels. Even with relatively low Be yields, there is still enough total Be present for AMS detection. Therefore, the extraction of cosmogenic  $^{10}\text{Be}$  from pyroxene samples using rapid fusion works well for samples with high  $^{10}\text{Be}$  concentrations. However, for the sample set that shows low  $^{10}\text{Be}$  concentrations, the measured concentrations are higher than expected by 320 000–810 000 atoms  $\text{g}^{-1}$ . We attribute this increased  $^{10}\text{Be}$  concentration to potential failure in completely removing all meteoric  $^{10}\text{Be}$  and/or a highly variable and poorly quantified procedural blank background correction.

Advances in measuring  $^{10}\text{Be}$  in pyroxene and constraints on the production rate provide new opportunities for multi-nuclide measurement in pyroxene-bearing samples that allow for correcting exposure ages for surface weathering and erosion and establishing exposure–burial histories.

**Code and data availability.** All data information associated with the cosmogenic nuclide measurements appears in tables. The exposure age and production rate calibration in the online exposure age calculator version 3 (<https://hess.ess.washington.edu>, Balco et al., 2008) has been updated to accept data from  $^{10}\text{Be}$  in pyroxene.

**Supplement.** The supplement related to this article is available online at: <https://doi.org/10.5194/gchron-6-491-2024-supplement>.

**Author contributions.** MB carried out sample preparation for unprocessed samples. MB and LBC performed beryllium extraction. MB and GB performed helium analysis, data reduction, and all data analyses. MB prepared the manuscript with contributions from all authors.

**Competing interests.** At least one of the (co-)authors is a member of the editorial board of *Geochronology*. The peer-review process was guided by an independent editor, and the authors also have no other competing interests to declare.

**Disclaimer.** Publisher's note: Copernicus Publications remains neutral with regard to jurisdictional claims made in the text, published maps, institutional affiliations, or any other geographical representation in this paper. While Copernicus Publications makes every effort to include appropriate place names, the final responsibility lies with the authors.

**Acknowledgements.** We would like to thank Allie Balter-Kennedy, Shaun Eaves, and Jamey Stutz for kindly providing the samples used for this study. Further, we thank Alan Hidy of the Center for Accelerator Mass Spectrometry at the Lawrence Livermore National Laboratory for providing the beryllium measurements. The Lawrence Livermore National Laboratory portion of this work was carried out under contract no. DE-AC52-07NA27344. This is LLNL-JRNL-861832.

**Financial support.** This research has been supported by the National Science Foundation (grant no. 2139497).

**Review statement.** This paper was edited by Hella Wittmann and reviewed by Samuel Niedermann and one anonymous referee.

## References

- Balco, G. and Rovey, C. W.: An isochron method for cosmogenic-nuclide dating of buried soils and sediments, *Am. J. Sci.*, 308, 1083–1114, <https://doi.org/10.2475/10.2008.02>, 2008.
- Balco, G. and Shuster, D. L.: Production rate of cosmogenic  $^{21}\text{Ne}$  in quartz estimated from  $^{10}\text{Be}$ ,  $^{26}\text{Al}$ , and  $^{21}\text{Ne}$  concentrations in slowly eroding Antarctic bedrock surfaces, *Earth Planet. Sc. Lett.*, 281, 48–58, <https://doi.org/10.1016/j.epsl.2009.02.006>, 2009.
- Balco, G., Stone, J. O., Lifton, N. A., and Dunai, T. J.: A complete and easily accessible means of calculating surface exposure ages or erosion rates from  $^{10}\text{Be}$  and  $^{26}\text{Al}$  measurements, *Quat. Geochronol.*, 3, 174–195, <https://doi.org/10.1016/j.quageo.2007.12.001>, 2008 (data available at: <https://hess.ess.washington.edu>, last access: 9 August 2024).
- Balco, G., DeJong, B. D., Ridge, J. C., Bierman, P. R., and Rood, D. H.: Atmospherically produced beryllium-10 in annually laminated late-glacial sediments of the North American Varve Chronology, *Geochronology*, 3, 1–33, <https://doi.org/10.5194/gchron-3-1-2021>, 2021.
- Balter-Kennedy, A., Bromley, G., Balco, G., Thomas, H., and Jackson, M. S.: A 14.5-million-year record of East Antarctic Ice Sheet fluctuations from the central Transantarctic Mountains, constrained with cosmogenic  $^3\text{He}$ ,  $^{10}\text{Be}$ ,  $^{21}\text{Ne}$ , and  $^{26}\text{Al}$ , *The Cryosphere*, 14, 2647–2672, <https://doi.org/10.5194/tc-14-2647-2020>, 2020.
- Balter-Kennedy, A., Schaefer, J. M., Schwartz, R., Lamp, J. L., Penrose, L., Middleton, J., Hanley, J., Tibari, B., Blard, P.-H., Winckler, G., Hidy, A. J., and Balco, G.: Cosmogenic  $^{10}\text{Be}$  in pyroxene: laboratory progress, production rate systematics, and application of the  $^{10}\text{Be}$ – $^3\text{He}$  nuclide pair in the Antarctic Dry Valleys, *Geochronology*, 5, 301–321, <https://doi.org/10.5194/gchron-5-301-2023>, 2023.
- Blard, P. H.: Cosmogenic  $^3\text{He}$  in terrestrial rocks: A review, *Chem. Geol.*, 586, 120543, <https://doi.org/10.1016/j.chemgeo.2021.120543>, 2021.
- Blard, P. H., Bourlès, D., Pik, R., and Lavé, J.: In situ cosmogenic  $^{10}\text{Be}$  in olivines and pyroxenes, *Quat. Geochronol.*, 3, 196–205, <https://doi.org/10.1016/j.quageo.2007.11.006>, 2008.
- Blard, P. H., Balco, G., Burnard, P. G., Farley, K. A., Fenton, C. R., Friedrich, R., Jull, A. J. T., Niedermann, S., Pik, R., Schaefer, J. M., Scott, E. M., Shuster, D. L., Stuart, F. M., Stute, M., Tibari, B., Winckler, G., and Zimmermann, L.: An inter-laboratory comparison of cosmogenic  $^3\text{He}$  and radiogenic  $^4\text{He}$  in the CRONUS-P pyroxene standard, *Quat. Geochronol.*, 26, 11–19, <https://doi.org/10.1016/j.quageo.2014.08.004>, 2015.
- Borchers, B., Marrero, S., Balco, G., Caffee, M., Goehring, B., Lifton, N., Nishiizumi, K., Phillips, F., Schaefer, J., and Stone, J.: Geological calibration of spallation production rates in the CRONUS-Earth project, *Quat. Geochronol.*, 31, 188–198, <https://doi.org/10.1016/j.quageo.2015.01.009>, 2016.
- Bromley, G., Balco, G., Jackson, M., Balter-Kennedy, A., and Thomas, H.: East Antarctic Ice Sheet Variability In The Central Transantarctic Mountains Since The Mid Miocene, *Clim. Past Discuss.* [preprint], <https://doi.org/10.5194/cp-2024-21>, in review, 2024.

- Collins, J. A.: In situ cosmogenic  $^{10}\text{Be}$  in pyroxene with an application to surface exposure dating, Master's thesis, Victoria University of Wellington, <https://doi.org/10.26686/wgtn.17013233.v1>, 2015.
- Corbett, L. B., Bierman, P. R., and Rood, D. H.: An approach for optimizing in situ cosmogenic  $^{10}\text{Be}$  sample preparation, *Quat. Geochronol.*, 33, 24–34, <https://doi.org/10.1016/j.quageo.2016.02.001>, 2016.
- Eaves, S. R., Collins, J. A., Jones, R. S., Norton, K. P., Tims, S. G., and Mackintosh, A. N.: Further constraint of the in situ cosmogenic  $^{10}\text{Be}$  production rate in pyroxene and a viability test for late Quaternary exposure dating, *Quat. Geochronol.*, 48, 121–132, <https://doi.org/10.1016/j.quageo.2018.09.006>, 2018.
- Elliot, D. H. and Fleming, T. H.: Chapter 2.1b Ferrar Large Igneous Province: petrology, Geological Society, London, *Memoirs*, 55, 93–119, <https://doi.org/10.1144/m55-2018-39>, 2021.
- Granger, D. E.: A review of burial dating methods using  $^{26}\text{Al}$  and  $^{10}\text{Be}$ , in: *In Situ-Produced Cosmogenic Nuclides and Quantification of Geological Processes*, edited by: Sime, L. L., Bourleŕs, D. L., and Brown, E. T., Geological Society of America, 1–16, [https://doi.org/10.1130/2006.2415\(01\)](https://doi.org/10.1130/2006.2415(01)), 2006.
- Granger, D. E. and Muzikar, P. F.: Dating sediment burial with in situ-produced cosmogenic nuclides: theory, techniques, and limitations, *Earth Planet. Sc. Lett.*, 188, 269–281, [https://doi.org/10.1016/s0012-821x\(01\)00309-0](https://doi.org/10.1016/s0012-821x(01)00309-0), 2001.
- Harvey, R. P.: The Ferrar Dolerite: An Antarctic analog for Martian basaltic lithologies and weathering processes, *Field Trip and Workshop on the Martian Highlands and Mojave Desert Analogs*, p. 25, 2001.
- Ivy-Ochs, S., Kubik, P. W., Masarik, J., Wieler, R., Bruno, L., and Schlŕchter, C.: Preliminary results on the use of pyroxene for  $^{10}\text{Be}$  surface exposure dating, *Schweizerische Mineralogische und Petrographische Mitteilungen*, 78, 375–382, 1998.
- Jull, A. J. T., Donahue, D. J., Linick, T. W., and Wilson, G. C.: Spallogenic  $^{14}\text{C}$  in High-Altitude Rocks and in Antarctic Meteorites, *Radiocarbon*, 31, 719–724, <https://doi.org/10.1017/S0033822200012315>, 1989.
- Kaplan, M. R., Licht, K. J., Winckler, G., Schaefer, J. M., Bader, N., Mathieson, C., Roberts, M., Kassab, C. M., Schwartz, R., and Graly, J. A.: Middle to Late Pleistocene stability of the central East Antarctic Ice Sheet at the head of Law Glacier, *Geology*, 45, 963–966, <https://doi.org/10.1130/g39189.1>, 2017.
- Klein, J., Giegengack, R., Middleton, R., Sharma, P., Underwood, J. R., and Weeks, R. A.: Revealing histories of exposure using in situ produced  $^{26}\text{Al}$  and  $^{10}\text{Be}$  in Libyan desert glass, *Radiocarbon*, 28, 547–555, <https://doi.org/10.1017/s0033822200007700>, 1986.
- Lal, D.: Cosmic ray labeling of erosion surfaces in situ nuclide production rates and erosion models, *Earth Planet. Sc. Lett.*, 104, 424–439, [https://doi.org/10.1016/0012-821X\(91\)90220-C](https://doi.org/10.1016/0012-821X(91)90220-C), 1991.
- Luna, L. V., Bookhagen, B., Niedermann, S., Rugel, G., Scharf, A., and Merchel, S.: Glacial chronology and production rate cross-calibration of five cosmogenic nuclide and mineral systems from the southern Central Andean Plateau, *Earth Planet. Sc. Lett.*, 500, 242–253, <https://doi.org/10.1016/j.epsl.2018.07.034>, 2018.
- Margerison, H. R., Phillips, W. M., Stuart, F. M., and Sugden, D. E.: Cosmogenic  $^3\text{He}$  concentrations in ancient flood deposits from the Coombs Hills, northern Dry Valleys, East Antarctica: interpreting exposure ages and erosion rates, *Earth Planet. Sc. Lett.*, 230, 163–175, <https://doi.org/10.1016/j.epsl.2004.11.007>, 2005.
- Masarik, J.: Numerical simulation of in-situ production of cosmogenic nuclides, Goldschmidt Conference, Davos, Switzerland, 2002, Abstract A491, <https://goldschmidtabstracts.info/abstracts/abstractView?id=2002001751> (last access: 9 August 2024), 2002.
- Niedermann, S., Schaefer, J., Wieler, R., and Naumann, R.: The production rate of cosmogenic  $^{38}\text{Ar}$  from calcium in terrestrial pyroxene, *Earth Planet. Sc. Lett.*, 257, 596–608, <https://doi.org/10.1016/j.epsl.2007.03.020>, 2007.
- Nishiizumi, K., Lal, D., Klein, J., Middleton, R., and Arnold, J. R.: Production of  $^{10}\text{Be}$  and  $^{26}\text{Al}$  by cosmic rays in terrestrial quartz in situ and implications for erosion rates, *Nature*, 319, 134–136, <https://doi.org/10.1038/319134a0>, 1986.
- Nishiizumi, K., Klein, J., Middleton, R., and Craig, H.: Cosmogenic  $^{10}\text{Be}$ ,  $^{26}\text{Al}$ , and  $^3\text{He}$  in olivine from Maui lavas, *Earth Planet. Sc. Lett.*, 98, 263–266, 1990.
- Nishiizumi, K., Imamura, M., Caffee, M. W., Southon, J. R., Finkel, R. C., and McAninch, J.: Absolute calibration of  $^{10}\text{Be}$  AMS standards, *Nuclear Instruments and Methods in Physics Research Section B: Beam Interactions with Materials and Atoms*, 258, 403–413, <https://doi.org/10.1016/j.nimb.2007.01.297>, 2007.
- Spector, P. and Balco, G.: Exposure-age data from across Antarctica reveal mid-Miocene establishment of polar desert climate, *Geology*, 49, 91–95, <https://doi.org/10.1130/g47783.1>, 2020.
- Stone, J.: A Rapid Fusion Method for Separation of Beryllium-10 From Soils and Silicates, *Geochim. Cosmochim. Ac.*, 62, 555–561, [https://doi.org/10.1016/s0016-7037\(97\)00340-2](https://doi.org/10.1016/s0016-7037(97)00340-2), 1998.
- Stone, J. O.: Air pressure and cosmogenic isotope production, *J. Geophys. Res.-Sol. Ea.*, 105, 23753–23759, <https://doi.org/10.1029/2000jb900181>, 2000.
- Stutz, J., Mackintosh, A., Norton, K., Whitmore, R., Baroni, C., Jamieson, S. S. R., Jones, R. S., Balco, G., Salvatore, M. C., Casale, S., Lee, J. I., Seong, Y. B., McKay, R., Vargo, L. J., Lowry, D., Spector, P., Christl, M., Ivy Ochs, S., Di Nicola, L., Iarossi, M., Stuart, F., and Woodruff, T.: Mid-Holocene thinning of David Glacier, Antarctica: chronology and controls, *The Cryosphere*, 15, 5447–5471, <https://doi.org/10.5194/tc-15-5447-2021>, 2021.